Insights from first principles molecular dynamics studies toward infrared multiple-photon and single-photon action spectroscopy: Case study of the proton-bound dimethyl ether dimer

Xiaohu Li,[1] David T. Moore,[2] and Srinivasan S. Iyengar[3,a)]

[1]*Department of Chemistry, Indiana University, 800 E. Kirkwood Ave., Bloomington, Indiana 47405, USA*
[2]*Department of Chemistry, Lehigh University, Bethlehem, Pennsylvania 18015, USA*
[3]*Department of Chemistry and Department of Physics, Indiana University, 800 E. Kirkwood Ave., Bloomington, Indiana 47405, USA*

We have used finite temperature *ab initio* molecular dynamics simulations in conjunction with computation of critical quantum nuclear effects to probe the differences between single-photon argon tagged action spectral results and infrared multiple-photon dissociation experiments for a proton bound molecular ion system. We find that the principal difference between the results in these experimental techniques is essentially that of cluster temperature. The multiple-photon dissociation experiments conducted using room temperature ions reflect a larger degree of conformational freedom compared to the colder single-photon argon tagged action spectral results. Our *ab initio* molecular dynamics simulation techniques accurately capture the effects of conformational sampling, adequately reproduce both spectra, and can be utilized to assign the dynamically averaged finite temperature spectra. © *2008 American Institute of Physics.* [DOI: 10.1063/1.2903446]

I. INTRODUCTION

In recent years, there has been great interest in the experimental[1–11] and theoretical[12–30] studies of hydrogen bonded cluster systems. For example, protonated, hydroxide as well as neutral water clusters have been studied in detail due to their fundamental role in biological[31–35] and condensed phase[36] chemical systems. In general, hydrogen bonded systems are of critical interest in a wide range of areas including materials,[37,38] atmospheric,[21,22,24–26,39–42] biological,[31–35] condensed phase,[43–46] and gas-phase cluster chemistry.[1,6,8–11,21,22,24–26]

Experimental studies on vibrational properties of hydrogen bonded cluster systems have blossomed due to the development of sophisticated cluster-based measurement techniques such as argon-tagged single photon action spectral methods[11,30] and the infrared multiple-photon dissociation[7,10,47–50] (IRMPD) approach. Both gas phase single-photon and multiple-photon vibrational action spectroscopic techniques have been crucial in deciphering the precise signatures that contribute to dynamics and spectroscopy in hydrogen bonded systems. However, the accurate computational modeling of the processes involved in these experiments requires the polarizability of the hydrogen bonding environment[7,8] and the changing bonding topography[6,21,22,28,29,44] to be considered, on account of the fluxional nature of hydrogen bonding systems. This renders the problem attractive to *ab initio* quantum mechanical treatment. There have been several theoretical methods utilized to treat such problems[1,6,8,21,22,25,26,28,29,51–62] with varying degrees of success. The issue is further complicated by the fact that single-photon and multiple-photon experiments, themselves seem to not always provide transparently consistent results in many cases.[7,8,10,11]

In this paper, we demonstrate how finite temperature *ab initio* molecular dynamics (AIMD) simulations can be utilized to model and understand single-photon argon-tagged vibrational spectral results as well as vibrational properties obtained from *noncoherent* multiple-photon dissociation processes. We consider here a case study of a proton bound diether: $(Me_2O)_2H^+$ [see Fig. 1(a)], which has recently been studied using both single photon[11] and multiple photon techniques.[10] This system is a prototypical organic system similar in form to the fundamental protonated Zundel cation, $H_5O_2^+$, which has been the subject of much recent experimental and theoretical debate.[6–8,27–30] The differences between the single-photon and multiple-photon experimental spectra for the Zundel cation,[6,7] seem similar to that in the diether system discussed here (see Figure 1(b)), but one might, *a priori*, expect the proton bound diether to be less complicated to simulate using theoretical models, on account of the expected lower coupling between the shared and peripheral protons that are now separated by a stable CO linkage. However, even here single- and multiple-photon experiments provide interesting differences that are analyzed in detail as part of this paper. The spectra in Fig. 1(b) are reproduced from previous experiments.[10,11] The IRMPD spectra are generally broad as compared to the single photon spectra obtained from argon tagging of the molecular ion. Furthermore, the single-photon experiment displays a doublet at ≈ 1000 cm^{-1}, which is not reproduced in harmonic treatment. This aspect is very much reminiscent of a similar result recently reported for the Zundel cation.[10,11,27] Both argon tagging and IRMPD are examples of action spectroscopy, based on fragmentation

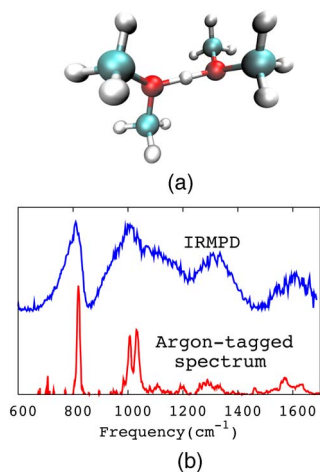a)Author to whom correspondence should be addressed. Electronic mail: iyengar@indiana.edu.

FIG. 1. (Color online) Vibrational action spectra for $[Me_2O-H-OMe_2]^+$ obtained from infrared multiple-photon dissociation [top panel of (b)], reproduced from Ref. 10, and argon-tagged single photon dissociation experiments [bottom panel of (b)], reproduced from Ref. 11. Note the broader distribution from IRMPD.

induced by the absorption of a single (Ar-tagging) or multiple (IRMPD) infrared photons. A major difference between these two techniques is the temperature of the ions involved in the experiments and this has an important effect on the observed spectral result. For example, the ions in an argon-tagged system are created in a supersonic molecular beam expansion and hence expected to be cold with an estimated effective temperature of the order of 100 K or lower.[11] The IRMPD spectra, on the other hand, were recorded from room temperature ions.[85] Here, we demonstrate the applicability of finite temperature AIMD as a computational tool that helps probe in detail, such complex spectroscopic differences, and resolve the spectra from both experimental situations. The central point is that we utilize AIMD to accumulate an ensemble-averaged vibrational spectrum representing statistical sampling of the conformational space explored by the ions at a given temperature, as has been previously shown.[21,22,25,26,56,63] At higher temperatures, some conformations may have significantly different vibrational frequencies than the global minimum, which manifests as *inhomogeneous broadening* with respect to the harmonic spectrum at the global minimum.

The paper is organized as follows: In Sec. II, the computational methods utilized are described. These include a blend of AIMD techniques, electronic structure optimizations and harmonic frequency calculations, analysis of the quantum nuclear structure of the shared proton, and an analysis of the intrinsic harmonic modes that contribute to the finite temperature spectrum obtained from dynamics. A discussion of results is provided in Sec. III and conclusions are given in Sec. IV.

II. COMPUTATIONAL METHODOLOGIES

A large number of simulations have been conducted as part of our study employing AIMD techniques, Born–Oppenheimer molecular dynamics (BOMD),[64–67] and atom-centered density matrix propagation (ADMP),[24,68–72] as

implemented within a development version of the Gaussian series of electronic structure codes.[73] These simulations utilize the B3LYP hybrid density functional with double-zeta polarized-diffused 6-31+G** basis, as suggested from previous studies[21,22,24–26,72,74,75] on similar systems. Geometry optimization and harmonic frequency calculations are performed to assist the decomposition and assignment of spectra obtained from finite temperature AIMD simulations. In addition, we have also investigated the quantum structure of the shared proton.

A time step of 0.5 fs was chosen for all BOMD dynamics studies while a fictitious mass-tensor scaling value of 0.1 amu bohr^2 ($\approx$180 a.u.) and a time step of 0.25 fs were used for ADMP. All AIMD simulations conducted here are microcanonical (NVE), with acceptable fluctuations (noted below) in the internal temperature. Since time-correlation functions involving nuclear velocities as well as molecular dipoles are utilized here to obtain vibrational properties, a constant energy simulation with an associated conserved Hamiltonian corresponding to the real system is critical. Two different sets of simulations were conducted, one corresponding to an average temperature of 68 K ($\pm$10 K), while the other corresponding to an average temperature of 270 K ($\pm$40 K). The lower temperature simulations are expected to model[21,22] the argon-tagged single-photon action spectrum experiments,[11] while the higher temperature simulations are expected to model the IRMPD experiments.[10] (This aspect is further discussed in Sec. III.) The dynamically averaged vibrational spectra were computed using Fourier transform of the nuclear velocity (represented as FT-VAC) and dipole (FT-DAC) autocorrelation functions. The results for BOMD and ADMP are qualitatively similar; hence, all data provided in the paper are from BOMD simulations.

A. Decomposition of the finite temperature AIMD spectra in terms of harmonic normal modes

It is relatively straightforward to assign the various peaks in a harmonic frequency calculation using eigenstates of the Hessian matrix computed at optimized classical nuclear geometries. In this section, we introduce an approach to decompose and assign the finite temperature dynamically averaged spectra obtained from the AIMD simulations. Since AIMD goes beyond the small oscillation limit of harmonic analysis, the results obtained from such a decomposition are in general different from standard normal mode analysis for cases dominated by anharmonic potentials (as is the case for the system treated here).

At frequency ω, the kth mass-weighted velocity component of the jth atom $\mathcal{V}_{j,k}$ contributes to the vibrational density of states as a result of its motion which may be expressed in frequency domain as

$$\widetilde{\mathcal{V}}_{j,k}(\omega) = \int dt \exp[-\iota\omega t]\mathcal{V}_{j,k}(t). \tag{1}$$

As per the convolution theorem,[76] the FT-VAC (and hence the vibrational density of states) is identical to the sum over all values of j and k of the power spectrum of Eq. (1). Now, the normal mode vectors, computed at some given geometry,

form a complete, orthonormal set since these are eigenstates of the Hessian matrix. [This includes the $(3N-6)$ vibrational modes as well as the six low-frequency modes, which are all considered together in the formal analysis in this section.] These vectors signify the direction and (small) amplitude motion of the N atoms within the harmonic approximation. Since the $3N$ dimensional vector $\vec{\tilde{\mathcal{V}}}(\omega)$, with components given by Eq. (1), also correspond to motion of the N atoms, but at a fixed frequency and finite temperature (since they are obtained from AIMD simulations), we may expand $\vec{\tilde{\mathcal{V}}}(\omega)$ in the basis of normal mode vectors as

$$\vec{\tilde{\mathcal{V}}}(\omega) = \sum_i C_i(\omega) * \vec{H}_i, \tag{2}$$

where $\vec{H}_i$ represents the ith normal mode vector and $C_i(\omega) = \vec{H}_i \cdot \vec{\tilde{\mathcal{V}}}(\omega)$ is the contribution of the ith normal mode vector toward nuclear motion at frequency ω during the finite temperature simulation. The net contribution of the ith normal mode to the vibrational density of states in the frequency range $[\omega_1, \omega_2]$ may then be written as a superposition of all its contributions inside the frequency range,

$$C_i^{[\omega_1,\omega_2]} = \left[\int_{\omega_1}^{\omega_2} d\omega |C_i(\omega)|^2 \right]^{1/2}$$
$$= \left[\int_{\omega_1}^{\omega_2} d\omega |\vec{H}_i \cdot \vec{\tilde{\mathcal{V}}}(\omega)|^2 \right]^{1/2}. \tag{3}$$

To compare contributions from all harmonic modes in a given frequency range, we analyze the quantity

$$C_i^{[\omega_1,\omega_2]} \Bigg/ \left[\sum_i \{C_i^{[\omega_1,\omega_2]}\}^2 \right] \tag{4}$$

in Sec. III. Equations (2) and (4) may be interpreted as follows. Equation (2) represents a standard projection of a $3N$ dimensional vector onto a complete orthonormal set of vectors. The components of Eq. (2) are then utilized in Eq. (4) to construct the *net* contribution of mode i in the frequency window $[\omega_1, \omega_2]$. This *net* contribution is essentially the L^2-norm of the ω-dependent function $\{C_i(\omega)\}$ for all $\omega \in [\omega_1, \omega_2]$. In practice, ω_1 and ω_2 are chosen to cover the relevant spectral feature which is determined upon inspection of the full FT-VAC and FT-DAC spectra. For illustrative purposes, we have noted the choice of ω_1 and ω_2 explicitly in tables later in the paper. Generally, these points are the closest local minima (or basins) that encompass the spectral feature of interest.

However, the contribution of mode i described in Eq. (4) is from the velocity spectrum and does not contain information about dipole (or IR) intensities. While all nuclear motions contribute to the FT-VAC, the dipole spectrum, which is provided in Sec. III, only contains those spectral features of the velocity spectrum that also have substantial dipole fluctuations (as in the experimental situation). To obtain the contribution from mode i to the dipole (or IR) spectrum, we utilize the harmonic IR intensities I_i as

$$D_i^{[\omega_1,\omega_2]} = I_i^{1/2} * C_i^{[\omega_1,\omega_2]}. \tag{5}$$

Again, to compare the relative contributions from all modes in a given frequency range, we analyze the ratio

$$D_i^{[\omega_1,\omega_2]} \Bigg/ \left[\sum_i \{D_i^{[\omega_1,\omega_2]}\}^2 \right] \tag{6}$$

in Sec. III. The quantity $|D_i^{[\omega_1,\omega_2]}|^2$ may be interpreted as being proportional to the "corrected IR intensity" at a given temperature. We utilize Eqs. (4) and (6) to probe the differences between the harmonic, high and low temperature results in Sec. III.

However, before we proceed with our discussion, we must note the following caveat: The decompositions described in Eqs. (2), (4), and (6) depend on the choice of the bases $\{\vec{H}_i\}$, and hence the choice of the optimized geometry. For our study on $[Me_2O-H-OMe_2]^+$, we have carefully analyzed over a hundred starting geometries to ensure that we have utilized the global minimum geometry in our analysis. For other general problems, an investigation of the $C_i^{[\omega_1,\omega_2]}$ and $D_i^{[\omega_1,\omega_2]}$ intensities for multiple optimized geometries may be necessary before physical conclusions can be derived from the analysis.

B. Shared proton nuclear quantum effects

To probe the effect of finite temperature on (nuclear) quantization of the shared proton in $[Me_2O-H-OMe_2]^+$, we obtain the shared proton eigenstates using its Hamiltonian in the coordinate representation,

$$H(x_i, x_j; \mathbf{R_C}) = -\frac{\hbar^2}{2m}\widetilde{K}_{k=2}(x_i, x_j) + V(x_i; \mathbf{R_C})\delta_{x_i,x_j}. \tag{7}$$

Here, the kinetic energy operator $\widetilde{K}_{k=2}(x_i, x_j)$ is represented in each dimension using distributed approximating functionals,[77–80]

$$\widetilde{K}_k(x_i, x_j) = \frac{1}{\sigma\sqrt{2\pi}}\left(\frac{-1}{\sqrt{2}\sigma}\right)^k$$
$$\times \exp\left(-\frac{(x_i - x_j)^2}{2\sigma^2}\right)$$
$$\times \sum_{n=0}^{M/2}\left(\frac{-1}{4}\right)^n \frac{1}{n!}H_{2n+k}\left(\frac{x_i - x_j}{\sqrt{2}\sigma}\right). \tag{8}$$

The index k defines the desired derivative, and hence $k=2$ for the Hamiltonian in Eq. (7). The H_{2n+k} are Hermite polynomials, $\{x_i\}$ is the coordinate representation of the (shared) quantum proton. $V(x_i; \mathbf{R_C})$ represents the hydrogen potential energy surface computed through hybrid density functional calculations performed on a three-dimensional grid of proton coordinates for chosen snapshots from the AIMD simulations. The quantity $\mathbf{R_C}$ represents the coordinates of all atoms apart from the shared proton. The dependence of $V(x_i; \mathbf{R_C})$ on $\mathbf{R_C}$ implies that the proton potential depends on

the geometry of the diether system and this aspect is probed by considering snapshots from the AIMD simulations. (A full dimensional quantum wave-packet propagation treatment of the 19-atom system treated here is currently prohibitive.) The representation in Eq. (8), however, leads to an extremely large (million×million) matrix representation for the quantum proton Hamiltonian. We obtain the lowest 30 quantum eigenstates by using a very efficient iterative Arnoldi iterative diagonalization scheme.[56,81–84]

The Arnoldi diagonalization process works as follows: First a random initial vector depicting the proton quantum state is obtained and the sequential action of the Hamiltonian on this starting vector is computed to obtain a family of basis vectors $\{\eta_i\}_{i=0,\ldots,M}$, where M is of the order of 100 (that is very much smaller than the size of the Hamiltonian matrix). The family of vectors $\{\eta_i\}_{i=0,\ldots,M}$ form a Krylov[83] basis. The Hamiltonian is then projected onto the Krylov basis to obtained a smaller $M \times M$ matrix which can be diagonalized easily to obtain the first few eigenstates of the proton. The complexity in this scheme scales as the matrix-vector product of the shared proton Hamiltonian matrix in Eq. (7) and the Krylov space vector. This action is greatly simplified by the fact that Eq. (8) represents a sparse, banded-Toeplitz matrix which allows for efficient $[\mathcal{O}(N)]$ matrix operations.

In Sec. III, we utilize the decomposition technique discussed in Sec. II A to assign the finite temperature spectral results and to probe the differences between the results at different temperatures. We also utilize the treatment of nuclear quantization discussed here, in Sec. II B, to provide a qualitative understanding of the effect of temperature on the spectrum.

III. RESULTS AND DISCUSSION

Harmonic frequencies, obtained at DFT (B3LYP) and MP2 optimized geometries, are presented on the top two panels of Figs. 2(a) and 2(b). As noted from the experimental spectra provided in the bottom panels of these figures, the harmonic calculations do not even qualitatively suggest a source for the observed broadening in the IRMPD spectrum. Furthermore, the doublet at 1000 cm^{-1} in the argon-tagged action spectrum [Fig. 2(b)] is also not reproduced by the harmonic calculation. This discrepancy is very similar to that encountered for the protonated Zundel cation, where again a doublet noted in the argon-tagged action spectrum experiment (at ~900 cm^{-1}) was not reproduced by harmonic analysis and by high level quantum calculations.[27] As we will see below, the underlying subtleties that dominate the Zundel cation also govern the fundamental organic, "Zundel-like" system [Me$_2$O−H−OMe$_2$]$^+$ treated here.

To understand the differences between the harmonic spectral results and the experimental calculations, we construct the Fourier transform of dipole and velocity autocorrelation functions (FT-DAC and FT-VAC) from AIMD data. The FT-DAC is presented using the curves labeled AIMD in Figs. 2(a) and 2(b). The FT-VAC is used later in this section to analyze and decompose the finite temperature spectra using the approach described in Sec. II A. The broad feature in the 1000−1200 cm^{-1} region in IRMPD is reproduced reason-
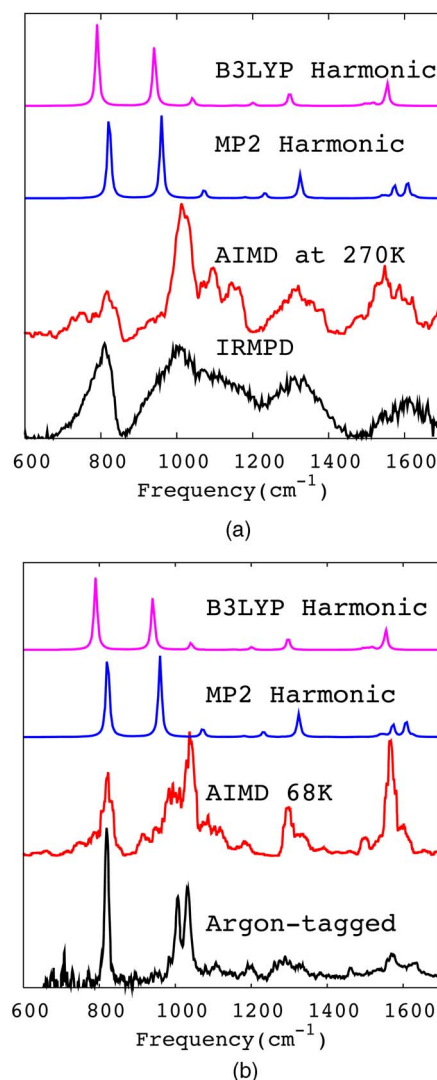

FIG. 2. (Color online) Finite temperature AIMD, IRMPD (reproduced from Ref. 10), argon-tagged single photon action spectrum experiments (reproduced from Ref. 11) and harmonic frequencies for (Me$_2$O)$_2$H$^+$.

ably well by the 270 K AIMD simulation. However, the additional features in the simulated results at 1000−1200 cm^{-1} seems to indicate that the effective temperature of the experiment is higher than 270 K, which may be consistent with previous studies.[85] The doublet at 1000 cm^{-1} in the argon-tagged spectrum is noted through a sharp peak at ~1038 cm^{-1} and a broader distribution at ~1000 cm^{-1} in the lower temperature simulation. In addition, the peaks at 1600 cm^{-1} have higher intensity in the 68 K simulation, which is not the case of the argon experiment. These aspects are probed here through a harmonic mode decomposition of the finite temperature spectra and further unraveled through a description of the quantum nuclear contributions from the shared proton.

In Tables I–V, we expand the finite temperature AIMD spectra using the harmonic normal modes (acquired at a minimum energy B3LYP structure) to obtain the coefficients $C_i^{[\omega_1,\omega_2]}$ and $D_i^{[\omega_1,\omega_2]}$, described in Eqs. (4) and (6). [While the results for $C_i^{[\omega_1,\omega_2]}$ and $D_i^{[\omega_1,\omega_2]}$ presented here were obtained using the B3LYP optimized geometry and frequencies, we

TABLE I. Analysis of the vibrational harmonic frequency components that contribute in the 800 cm^{-1} region for both low (68 K) and high temperature (270 K) AIMD spectra. The normal modes are described in the Appendix. The decomposition coefficients obtained from Eqs. (4) and (6), i.e., ($C_i^{[\omega_1,\omega_2]}$ and $D_i^{[\omega_1,\omega_2]}$), are both provided; $D_i^{[\omega_1,\omega_2]}$ inside the parentheses. (Threshold for both coefficients are chosen to be 0.15 in all tables.) The light modes, designated as those having relatively high $D_i^{[\omega_1,\omega_2]}$ intensities, are boldface.

	Harmonic mode decompositions (at 800 cm^{-1})[a]				
68 K	**0.85** **(0.93)** $H_{788}^{\mathrm{OPO}_{A\text{-}S}-\mathrm{COC}_{S\text{-}S}}$ +	**0.38** **(0.36)** $H_{940}^{P_\parallel-\mathrm{COC}_{S\text{-}S}}$ +	0.17 (0.0047) $H_{932}^{\mathrm{OO}_S-\mathrm{COC}_{S\text{-}S}}$		
270 K	**0.66** **(0.87)** $H_{788}^{\mathrm{OPO}_{A\text{-}S}-\mathrm{COC}_{S\text{-}S}}$ +	**0.42** **(0.47)** $H_{940}^{P_\parallel-\mathrm{COC}_{S\text{-}S}}$ +	0.24 (0.0084) $H_{932}^{\mathrm{OO}_S-\mathrm{COC}_{S\text{-}S}}$ +	0.18 (0.0023) $H_{32}^{\mathrm{ether}_{A}\text{-twist}}$ +	0.17 (0.005) $H_{536}^{\mathrm{OO}_S-\mathrm{COC}_{S\text{-}S}}$

[a]Note that $\omega_1 = 682$ cm^{-1} and $\omega_2 = 863$ cm^{-1}.

have also conducted a similar analysis by using the MP2 optimized geometry and frequencies and found good qualitative agreement between the two results.] The notation used in Tables I–V, to represent the normal modes, is discussed in the Appendix. Generally, the normal modes are represented as $H_{\mathrm{subscript}}^{\mathrm{superscript}}$, where the subscript indicates the actual normal mode frequency and the superscript is a notation utilized to describe the atomic motions that constitute the mode (see Appendix). This decomposition facilitates an analysis of the normal mode couplings involved in the finite temperature simulations and provides a chemical interpretation for the finite temperature spectrum in terms of the intrinsic harmonic modes. In addition, while the analysis in Sec. II A considers a complete set of harmonic mode vectors, which includes all $3N$ harmonic modes, it was found that the highest contributions in Tables I–V arise from the $(3N-6)$ internal modes. In addition, the mode decompositions at different frequencies are not expected to be orthogonal. That is,

$$\sum_i C_i^{[\omega_1,\omega_2]} \cdot C_i^{[\omega_3,\omega_4]}$$

$$= \left[\int_{\omega_1}^{\omega_2} d\omega |C_i(\omega)|^2\right]^{1/2} \cdot \left[\int_{\omega_3}^{\omega_4} d\omega' |C_i(\omega')|^2\right]^{1/2} \geq 0.$$

(9)

Hence, the analysis here does not provide effective eigenstates at a given temperature but provides a qualitative description of the normal mode couplings that yield the finite temperature spectrum.

Before we embark upon a detailed analysis of Tables I–V, there are a few general features that we must highlight. First and foremost, we find that both "light" and "dark" modes (i.e., absorbing and nonabsorbing modes) contribute to the intensities displayed in Tables I–V. The light modes are characterized by the larger $D_i^{[\omega_1,\omega_2]}$ values, which are presented in parentheses in the tables. The dark modes have lower contributions from $D_i^{[\omega_1,\omega_2]}$ and higher contributions from $C_i^{[\omega_1,\omega_2]}$. (In Tables I–V, the light modes with relatively high $D_i^{[\omega_1,\omega_2]}$ intensities are shown in boldface.) The dark modes contribute to the respective spectra through intensity borrowing via intramolecular vibrational redistribution (IVR) from the light modes. It is further clear upon inspection of all tables that there are four major light modes present in both high and low temperature calculations: $H_{788}^{\mathrm{OPO}_{A\text{-}S}-\mathrm{COC}_{S\text{-}S}}$, $H_{940}^{P_\parallel-\mathrm{COC}_{S\text{-}S}}$, $H_{1297}^{\mathrm{OPO}_{A\text{-}S}-\mathrm{CH_3rock}-\mathrm{COC}_{\mathrm{scissor}}}$, and $H_{1555}^{P_\nwarrow+\mathrm{CH_3}S\text{-scissor}}$. As

per the notation described in the Appendix, the mode designated as $H_{788}^{\mathrm{OPO}_{A\text{-}S}-\mathrm{COC}_{S\text{-}S}}$ couples an antisymmetric triatomic stretch mode involving the shared proton and the two oxygen atoms (designated as $\mathrm{OPO}_{A\text{-}S}$) with the symmetric triatomic stretch mode involving the carbons and oxygens ($\mathrm{COC}_{S\text{-}S}$) and occurs at 788 cm^{-1} in the harmonic calculation. Similarly, $H_{940}^{P_\parallel-\mathrm{COC}_{S\text{-}S}}$ involves a large amplitude shared proton stretch coupled to the ether backbone symmetric stretch. The mode designated as $H_{1297}^{\mathrm{OPO}_{A\text{-}S}-\mathrm{CH_3rock}-\mathrm{COC}_{\mathrm{scissor}}}$ involves the $\mathrm{OPO}_{A\text{-}S}$ antisymmetric triatomic stretch mode coupled to methyl rock and ether backbone scissor motion, whereas the mode $H_{1555}^{P_\nwarrow+\mathrm{CH_3}S\text{-scissor}}$ includes the shared proton motion, directed away from the oxygen-oxygen axis at an angle of 50°, coupled to a scissor or umbrella motion of the methyl groups. As expected, these are the same major modes that are displayed with highest IR intensity in the harmonic spectra in Figs. 2(a) and 2(b). All of these modes include contributions from the shared proton stretch, on account of the large dipole modulation associated with such a (polarizing) motion. In addition, there are two modes, $H_{1041}^{\mathrm{COC}_{A\text{-}S}-P_\perp}$ and $H_{1201}^{\mathrm{ether_{wag}}-P_\parallel}$, that have lower intensities in Figs. 2(a) and 2(b). These modes contribute as light modes in Tables I–V whenever the corresponding velocity coefficients $C_i^{[\omega_1,\omega_2]}$ are large. Second, we find that the band at ≈800 cm^{-1} has "innate intensity" in both high and low temperature simulations since this is the spectral region where the modes having high $C_i^{[\omega_1,\omega_2]}$ values also have high $D_i^{[\omega_1,\omega_2]}$ values. The rest of the spectral features have a relatively higher contribution from borrowed intensity. Furthermore, the coefficients for the dark modes grow as a function of temperature as we see in our discussion below.

In Table I, we provide the mode decompositions for the low end of the spectral region. Both $C_i^{[\omega_1,\omega_2]}$ and $D_i^{[\omega_1,\omega_2]}$ coefficients are provided; $D_i^{[\omega_1,\omega_2]}$ are provided within parentheses. We only provide modes with $C_i^{[\omega_1,\omega_2]} \geq 0.15$, however Fig. 3 lists the contributions from all harmonic modes. This is coupled to minor contributions from symmetric C–O–C backbone stretch motion and O–O stretch. The mode designated as $H_{788}^{\mathrm{OPO}_{A\text{-}S}-\mathrm{COC}_{S\text{-}S}}$ and $H_{940}^{P_\parallel-\mathrm{COC}_{S\text{-}S}}$ constitute the predominant contribution in this spectral region for high as well as low temperature simulations. A relatively minor contribution arises in both cases from the coupled motion of the oxygen-oxygen stretch with the COC symmetric stretch. Importantly, the results from decomposition of both FT-VAC and FT-DAC are consistent in the sense that the coefficients
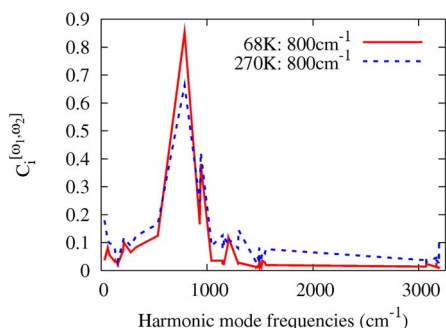
FIG. 3. (Color online) Distribution of $C_i^{[\omega_1,\omega_2]}$ for the 800 cm^{-1} band for low and high temperature simulations. Note that these plots are only defined for discrete values of the horizontal axis, i.e., only at the harmonic frequencies, which explains why the plots are piecewise linear.

$C_i^{[\omega_1,\omega_2]}$ and $D_i^{[\omega_1,\omega_2]}$ are both equally significant in magnitude for the most dominant modes in this region of the spectrum, which as we see below is not the case for the other spectral regions. Furthermore, as noted in Fig. 3, the critical modes that contribute to both high and low temperature simulations through $C_i^{[\omega_1,\omega_2]}$ intensities are basically the same, although the distribution of intensities for the higher temperature simulation is slightly broad as compared to the low temperature simulation. In addition, it may be noted from Fig. 3 that the two modes displaying the lowest $C_i^{[\omega_1,\omega_2]}$ intensities in Table I at 270 K are only slight lower in intensity at 68 K. These results may also be compared to recent experiments[10,50] on a variety of proton bound ether systems where it is noted that the nature of the 800 cm^{-1} feature is roughly conserved over a progression of ether groups studied.

Results in the $1000-1200$ cm^{-1} region are provided in Tables II and III. In this frequency range, the velocity and dipole contributions are not uniform and modes that have a high contribution in the velocity spectrum (characterized by the larger values of $C_i^{[\omega_1,\omega_2]}$) may have a far lower dipole contribution. For example, the coupled O–O stretch, C–O–C symmetric stretch mode has the most significant velocity contribution at 1000 cm^{-1} in the 68 K result (Table II). However, the corresponding dipole intensity is very weak. The proton stretch features $H_{788}^{OPO_{A-S}-COC_{S-S}}$ and $H_{940}^{P_\parallel-COC_{S-S}}$, however, always display a high dipole intensity. In addition, the

weak $H_{1041}^{COC_{A-S}-P_\perp}$ mode contributes on account of a large $C_i^{[\omega_1,\omega_2]}$ value. As noted before, the sharp doublet in the argon-tagged action spectrum is fundamentally different from the harmonic spectrum in Fig. 2(b). The finite temperature simulation reproduces the doublet through the features at 1000 and 1038 cm^{-1} which are analyzed in Table II. The two features are similar and display similar sharp IR intensities, on account of contributions from proton stretch modes $H_{788}^{OPO_{A-S}-COC_{S-S}}$ and $H_{940}^{P_\parallel-COC_{S-S}}$ but differ through contributions from OO stretch and COC symmetric stretch at 1000 cm^{-1} and methyl wag at 1038 cm^{-1}. This aspect is also clear from Fig. 4(a), where the distribution of $C_i^{[\omega_1,\omega_2]}$ intensities is presented. This illustrates the coupling between the shared proton stretch and the motion of peripheral atoms. These results are to be compared with recent studies involving multiconfigurational time-dependent Hartree calculations on the Zundel cation,[27] where it was noted that the coupling between the OH wag motion from the participating water molecules and the shared proton stretch are responsible for splitting the 900 cm^{-1} singlet peak noted earlier in harmonic calculations, vibrational configuration interaction, and quantum Monte Carlo studies.[8] Here, again we note a similar contribution from the COC symmetric stretch and the methyl wag, in the most fundamental organic Zundel-like system $[Me_2O-H-OMe_2]^+$, which results in a splitting of the sharp singlet at 940 cm^{-1} reported in the harmonic spectrum. This is, however, not a surprise since in larger, more general proton donor-acceptor systems (such as those occurring in many enzymes[86]), this kind of coupled motion is responsible for secondary isotope effects. Hence, it will be interesting to investigate the dependence of such complex, coupled motions in the generic $[R_2O-H-OR_2']^+$ systems for different R and R' groups at low temperature. This will be explored in future publications.

From Table III we note a striking similarity between the modes that contribute to the 1012 and 1095 cm^{-1} regions in the 270 K spectrum and the 1000 and 1038 cm^{-1} regions in the 68 K result. However, as is clear from Table III and also from Fig. 4(b), there are far greater numbers of harmonic modes that contribute to the high temperature spectrum as compared to the lower temperature spectrum. For example, as shown in Fig. 4(b), the high temperature distribution around 1000 cm^{-1} is broader than the low temperature dis-

TABLE II. Analysis of the vibrational harmonic frequency components that contribute in the $1000-1200$ cm^{-1} region for the low temperature (68 K) AIMD spectra. The normal modes are described in the Appendix. The decomposition coefficients obtained from Eqs. (4) and (6), i.e., $C_i^{[\omega_1,\omega_2]}$ and $D_i^{[\omega_1,\omega_2]}$, are both provided; $D_i^{[\omega_1,\omega_2]}$ inside the parentheses. (Threshold for both coefficients are chosen to be 0.15 in all tables.) The light modes, designated as those having relatively high $D_i^{[\omega_1,\omega_2]}$ intensities, are boldface.

	68 K
Frequency	Harmonic mode decompositions
1000 cm^{-1a}	$\begin{matrix}0.77\\(0.045)\end{matrix} H_{932}^{OO_S-COC_{S-S}} + \begin{matrix}\mathbf{0.49}\\\mathbf{(0.93)}\end{matrix} \mathbf{H_{940}^{P_\parallel-COC_{S-S}}} + \begin{matrix}\mathbf{0.15}\\\mathbf{(0.34)}\end{matrix} \mathbf{H_{788}^{OPO_{A-S}-COC_{S-S}}} + \begin{matrix}0.15\\(0.072)\end{matrix} H_{1041}^{COC_{A-S}-P_\perp}$
1038 cm^{-1b}	$\begin{matrix}\mathbf{0.69}\\\mathbf{(0.44)}\end{matrix} \mathbf{H_{1041}^{COC_{A-S}-P_\perp}} + \begin{matrix}0.51\\(0.061)\end{matrix} H_{1147}^{CH_{3}wag-P_\perp} + \begin{matrix}\mathbf{0.32}\\\mathbf{(0.79)}\end{matrix} \mathbf{H_{940}^{P_\parallel-COC_{S-S}}} + \begin{matrix}\mathbf{0.14}\\\mathbf{(0.40)}\end{matrix} \mathbf{H_{788}^{OPO_{A-S}-COC_{S-S}}}$

[a] $\omega_1=875$ cm^{-1} and $\omega_2=1015$ cm^{-1}.
[b] $\omega_1=1015$ cm^{-1} and $\omega_2=1147$ cm^{-1}.

TABLE III. Analysis of the vibrational harmonic frequency components that contribute in the 1000–1200 cm^{-1} region for the high temperature (270 K) AIMD spectra. The normal modes are described in the Appendix. The decomposition coefficients obtained from Eqs. (4) and (6), i.e., $C_i^{[\omega_1,\omega_2]}$ and $D_i^{[\omega_1,\omega_2]}$, are both provided; $D_i^{[\omega_1,\omega_2]}$ inside the parentheses. (Threshold for both coefficients are chosen to be 0.15 in all tables.) The light modes, designated as those having relatively high $D_i^{[\omega_1,\omega_2]}$ intensities, are boldface.

Frequency	270 K
	Harmonic mode decompositions
1012 cm^{-1}[a]	$\mathbf{0.67}$ $(\mathbf{0.48})$ $H_{\mathbf{1041}}^{\mathbf{COC}_{A\text{-}S}\text{-}P_\perp}$ + $\dfrac{0.45}{(0.038)}$ $H_{932}^{OO_S\text{-}COC_{S\text{-}S}}$ + $\mathbf{0.28}$ $(\mathbf{0.79})$ $H_{\mathbf{940}}^{P_\parallel\text{-}\mathbf{COC}_{S\text{-}S}}$
1095 cm^{-1}[b]	$\mathbf{0.47}$ $(\mathbf{0.87})$ $H_{\mathbf{940}}^{P_\parallel\text{-}\mathbf{COC}_{S\text{-}S}}$ + $\mathbf{0.33}$ $(\mathbf{0.16})$ $H_{\mathbf{1041}}^{\mathbf{COC}_{A\text{-}S}\text{-}P_\perp}$ + $\dfrac{0.26}{(0.025)}$ $H_{1147}^{CH_{3}wag\text{-}P_\perp}$ + $\dfrac{0.25}{(0.024)}$ $H_{1157}^{CH_{3S}\text{-}wag}$ + $\mathbf{0.19}$ $(\mathbf{0.41})$ $H_{\mathbf{788}}^{OPO_{A\text{-}S}\text{-}COC_{S\text{-}S}}$ + $\dfrac{0.19}{(0.078)}$ $H_{1201}^{ether_{wag}\text{-}P_\parallel}$ + $\dfrac{0.16}{(0.066)}$ $H_{1521}^{P_\perp}$ + $\dfrac{0.15}{(0.044)}$ $H_{1547}^{P_\perp}$ + $\dfrac{0.15}{(0.016)}$ $H_{1194}^{ether_{wag}}$
1155 cm^{-1}[c]	$\dfrac{0.30}{(0.060)}$ $H_{1194}^{ether_{wag}}$ + $\dfrac{0.38}{(0.068)}$ $H_{1157}^{CH_{3S}\text{-}wag}$ + $\dfrac{0.35}{(0.061)}$ $H_{1147}^{CH_{3}wag\text{-}P_\perp}$ + $\mathbf{0.28}$ $(\mathbf{0.22})$ $H_{\mathbf{1201}}^{\mathbf{Ether}_{wag}\text{-}P_\parallel}$ + $\mathbf{0.21}$ $(\mathbf{0.35})$ $H_{\mathbf{1297}}^{OPO_{A\text{-}S}\text{-}CH_3\mathbf{rock}\text{-}COC_{scissor}}$ + $\dfrac{0.24}{(0.026)}$ $H_{3192}^{CH_{stretch}}$ + $\dfrac{0.17}{(0.030)}$ $H_{1294}^{OO_S\text{-}CH_3wag}$ + $\dfrac{0.17}{(0.021)}$ $H_{1497}^{CH_{3A}\text{-}scissor\text{-}P_\perp}$ + $\mathbf{0.15}$ $(\mathbf{0.63})$ $H_{\mathbf{788}}^{OPO_{A\text{-}S}\text{-}COC_{S\text{-}S}}$ + $\dfrac{0.15}{(0.044)}$ $H_{1494}^{CH_{3S}\text{-}scissor\text{-}P_\perp}$ + $\mathbf{0.15}$ $(\mathbf{0.53})$ $H_{\mathbf{940}}^{P_\parallel\text{-}\mathbf{COC}_{S\text{-}S}}$

[a]$\omega_1 = 863$ cm^{-1} and $\omega_2 = 1055$ cm^{-1}.
[b]$\omega_1 = 1055$ cm^{-1} and $\omega_2 = 1118$ cm^{-1}.
[c]$\omega_1 = 1118$ cm^{-1} and $\omega_2 = 1200$ cm^{-1}.

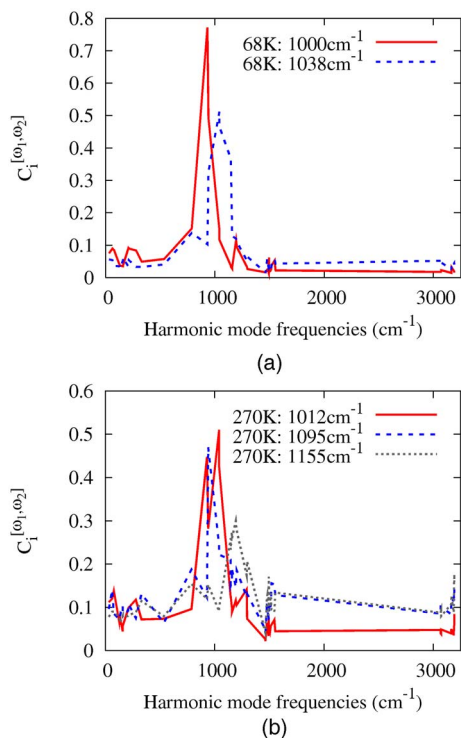FIG. 4. (Color online) Distribution of $C_i^{[\omega_1,\omega_2]}$ for the 1000–1200 cm^{-1} band for low (a) and high (b) temperature simulations. Note that these plots are only defined for discrete values of the horizontal axis, i.e., only at the harmonic frequencies, which explains why the plots are piecewise linear.
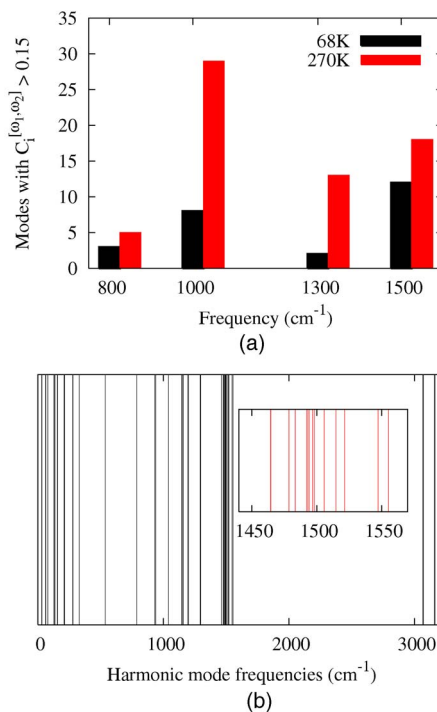

FIG. 5. (Color online) The distribution of harmonic modes for low and high temperature simulations is shown in (a). The vertical axis in (a) represents the number of states that contribute to the velocity spectrum with $C_i^{[\omega_1,\omega_2]}$ >0.15. The relatively higher population for the 1500 cm^{-1} band at 68 K is due to the large density of harmonic mode states in this region. See (b) for a representation of the density of harmonic modes. More than a fourth of the $(3N-6)$ harmonic modes appear inside the 1450–1550 cm^{-1} window shown in the inset of (b).

TABLE IV. Analysis of the vibrational harmonic frequency components that contribute in the 1300 cm^{-1} region for both low temperature (68 K) and high temperature (270 K) AIMD spectra. The normal modes are described in the Appendix. The decomposition coefficients obtained from Eqs. (4) and (6), i.e., $C_i^{[\omega_1,\omega_2]}$ and $D_i^{[\omega_1,\omega_2]}$, are both provided; $D_i^{[\omega_1,\omega_2]}$ inside the parentheses. (Threshold for both coefficients are chosen to be 0.15 in all tables.) The light modes, designated as those having relatively high $D_i^{[\omega_1,\omega_2]}$ intensities, are boldface.

Frequency	Harmonic mode decompositions
	68 K
1300 cm^{-1a}	$\begin{matrix}0.68\\(0.10)\end{matrix} H_{1294}^{\text{OO}_S-\text{CH}_3\text{wag}} + \begin{matrix}\mathbf{0.62}\\\mathbf{(0.90)}\end{matrix} H_{1297}^{\mathbf{OPO}_{A-S}-\mathbf{CH_3 rock-COC_{scissor}}}$
	270 K
1320 cm^{-1b}	$\begin{matrix}0.36\\(0.057)\end{matrix} H_{1294}^{\text{OO}_S-\text{CH}_3\text{wag}} + \begin{matrix}\mathbf{0.32}\\\mathbf{(0.50)}\end{matrix} H_{1297}^{\mathbf{OPO}_{A-S}-\mathbf{CH_3 rock-COC_{scissor}}} + \begin{matrix}0.24\\(0.12)\end{matrix} H_{1547}^{P_\perp} + \begin{matrix}0.30\\(0.045)\end{matrix} H_{1147}^{\text{CH}_3\text{wag}-P_\perp}$
	$+ \begin{matrix}0.27\\(0.024)\end{matrix} H_{3192}^{\text{CH}_{\text{stretch}}} + \begin{matrix}0.20\\(0.15)\end{matrix} H_{1521}^{P_\perp} \begin{matrix}0.17\\(0.13)\end{matrix} H_{1201}^{\text{ether wag}-P_\parallel} + \begin{matrix}0.22\\(0.038)\end{matrix} H_{1157}^{\text{CH}_3 S-\text{wag}}$
	$+ \begin{matrix}\mathbf{0.16}\\\mathbf{(0.50)}\end{matrix} H_{940}^{P_\parallel-\text{COC}_{S-S}} + \begin{matrix}\mathbf{0.15}\\\mathbf{(0.57)}\end{matrix} H_{788}^{\mathbf{OPO}_{A-S}-\mathbf{COC}_{S-S}}$

[a] $\omega_1=1270$ cm^{-1} and $\omega_2=1367$ cm^{-1}.
[b] $\omega_1=1200$ cm^{-1} and $\omega_2=1418$ cm^{-1}.

tribution in Fig. 4(a), with significant contributions from the low as well as high ends of the spectral region.

The higher frequency mode in Table III displays contributions from modes such as the ether wag, COC scissor motion, and methyl symmetric wag, which are not seen in any of the lower spectral regions both at high and low temperatures. Furthermore, the higher frequency mode in Table III mostly contains "dark" modes, which are characterized by large $C_i^{[\omega_1,\omega_2]}$ values and relatively small $D_i^{[\omega_1,\omega_2]}$ values. This implies that the 1155 cm^{-1} peak in the 270 K simulation mostly appears due to intensity borrowing from the light $H_{1297}^{\text{OPO}_{A-S}-\text{CH}_3\text{rock}-\text{COC}_{\text{scissor}}}$ mode. As the temperature is increased, the portion of the potential surface that is sampled during dynamics may become highly anharmonic, resulting in the coupling of many harmonic modes. This is essentially on display for the broad feature extending up to 1200 cm^{-1} for the higher temperature simulated spectrum and is consistent with the interpretation that the broader spectral features in the IRMPD spectrum recorded in Ref. 10 result from the intrinsic higher temperature of the ions. To further probe this

aspect, we present in Fig. 5(a) the number of contributing normal modes with $C_i^{[\omega_1,\omega_2]}>0.15$ for the high and low temperature AIMD simulations. Clearly, the higher temperature simulation is dictated by a far greater number of harmonic modes as compared to the low temperature result. This can also be seen from the data in Table IV, which show that the same principal modes contribute to the 1300 cm^{-1} region of both the 68 and 270 K simulations, but that the higher-temperature spectrum also has contributions from many more dark modes, as well as two additional light modes. Furthermore, it is clear that essentially all of the intensity between 800 and 1300 cm^{-1} in both simulated spectra is derived from the three light modes involving the stretching motion of the shared proton (Figs. 6 and 7).

On the other hand, the spectral decomposition in Table V indicates no contribution from the shared proton stretch and is complicated by the large density of harmonic normal mode states at around 1500 cm^{-1} [see Fig. 5(b)] and all of these modes contribute even for the low temperature case. This is also noted in Fig. 5(a) by the relatively larger number of
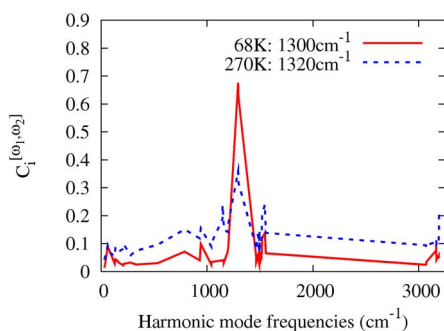

FIG. 6. (Color online) Distribution of $C_i^{[\omega_1,\omega_2]}$ for the 1300 cm^{-1} band for low and high temperature simulations. Note that these plots are only defined for discrete values of the horizontal axis, i.e., only at the harmonic frequencies, which explains why the plots are piecewise linear.
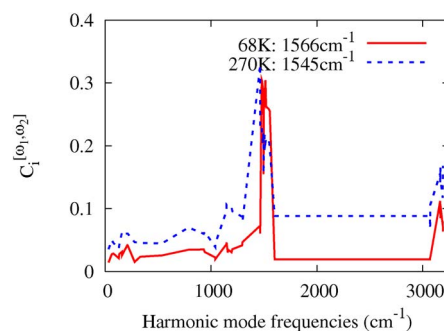
FIG. 7. (Color online) Distribution of $C_i^{[\omega_1,\omega_2]}$ for the 1300 cm^{-1} band for low and high temperature simulations. Note that these plots are only defined for discrete values of the horizontal axis, i.e., only at the harmonic frequencies, which explains why the plots are piecewise linear.

TABLE V. Analysis of the vibrational harmonic frequency components that contribute in the 1500 cm^{-1} region for both low temperature (68 K) and high temperature (270 K) AIMD spectra. The normal modes are described in the Appendix. The decomposition coefficients obtained from Eqs. (4) and (6), i.e., $C_i^{[\omega_1,\omega_2]}$ and $D_i^{[\omega_1,\omega_2]}$, are both provided; $D_i^{[\omega_1,\omega_2]}$ inside the parentheses. (Threshold for both coefficients are chosen to be 0.15 in all tables.) The light modes, designated as those having relatively high $D_i^{[\omega_1,\omega_2]}$ intensities, are boldface.

Frequency	Harmonic mode decompositions
	68 K
1566 cm^{-1}[a]	$\dfrac{0.31}{(0.049)} H_{1479}^{CH_3A\text{-scissor}-P_\perp} + \dfrac{0.30}{(0.17)} H_{1515}^{CH_3S\text{-scissor}-P_\perp} + \dfrac{0.30}{(0.054)} H_{1483}^{CH_3\text{scissor-rock}-P_\perp} + \dfrac{0.29}{(0.091)} H_{1492}^{CH_3S\text{-umbrella}} + \dfrac{0.29}{(0.12)} H_{1494}^{CH_3S\text{-scissor}-P_\perp}$
	$+ \dfrac{0.28}{(0.11)} H_{1498}^{CH_3A\text{-scissor}-P_\perp} + \dfrac{0.28}{(0.19)} H_{1493}^{CH_3\text{scissor-rock}} + \dfrac{0.27}{(0.20)} H_{1506}^{CH_3\text{scissor-rock}-P_\perp} + \dfrac{0.26}{(0.31)} H_{1521}^{P_\perp}$
	$+ \dfrac{0.26}{(0.21)} H_{1547}^{P_\perp} + \dfrac{\mathbf{0.26}}{\mathbf{(0.79)}} \mathbf{H_{1555}^{P_\searrow + CH_3S\text{-scissor}}} + \dfrac{0.16}{(0.029)} H_{1497}^{CH_3A\text{-scissor}-P_\perp}$
	270 K
1545 cm^{-1}[b]	$\dfrac{0.40}{(0.10)} H_{1464}^{CH_3A\text{-umbrella}-P_\perp} + \dfrac{0.23}{(0.039)} H_{1479}^{CH_3A\text{-scissor}-P_\perp} + \dfrac{0.22}{(0.15)} H_{1493}^{CH_3\text{scissor-rock}} + \dfrac{0.22}{(0.16)} H_{1506}^{CH_3\text{scissor-rock}-P_\perp} + \dfrac{0.22}{(0.041)} H_{1483}^{CH_3\text{scissor-rock}-P_\perp}$
	$+ \dfrac{0.21}{(0.26)} H_{1521}^{P_\perp} + \dfrac{0.21}{(0.17)} H_{1547}^{P_\perp} + \dfrac{0.21}{(0.090)} H_{1494}^{CH_3S\text{-scissor}-P_\perp} + \dfrac{0.21}{(0.12)} H_{1515}^{CH_3S\text{-scissor}-P_\perp} + \dfrac{0.20}{(0.066)} H_{1492}^{CH_3S\text{-umbrella}}$
	$+ \dfrac{\mathbf{0.20}}{\mathbf{(0.63)}} \mathbf{H_{1555}^{P_\searrow + CH_3S\text{-scissor}}} + \dfrac{0.19}{(0.077)} H_{1498}^{CH_3A\text{-scissor}-P_\perp} + \dfrac{0.17}{(0.039)} H_{3192}^{CH\text{stretch}} + \dfrac{0.17}{(0.0057)} H_{3166}^{A-CH\text{stretch}}$
	$+ \dfrac{0.16}{(0.030)} H_{1497}^{CH_3A\text{-scissor}-P_\perp} + \dfrac{0.16}{(0.055)} H_{3163}^{S-CH\text{stretch}}$

[a] $\omega_1 = 1478$ cm^{-1} and $\omega_2 = 1630$ cm^{-1}.
[b] $\omega_1 = 1418$ cm^{-1} and $\omega_2 = 1664$ cm^{-1}.

modes contributing to the low temperature spectrum at 1500 cm^{-1}, as compared to other frequency ranges. This aspect is also indicative of the fact that the effective temperature of the argon tagged experiments may be lower than 68 K. As a result, lower temperature AIMD simulations are currently in progress to further refine this region of the spectrum.

The preceding results provide a detailed description of the mechanism of spectral broadening at high temperatures, *namely*, the anharmonic coupling between harmonic vibrational modes and intensity borrowing between light and dark modes. In the next section, we will study the nuclear quantum nature of the "soft" shared proton mode and present another qualitative explanation for the spectral broadening in terms of the intrinsic potential energy surface experienced by the shared proton. However, it is already clear that first principles, finite temperature molecular dynamics can provide insights into argon-tagged single photon as well as multiple photon experimental processes. While this has been noted previously[21,22,25,56,63] for argon-tagged single photon experiments, the result is relatively new with respect to the multiple photon (IRMPD) experimental situation. With regards to comparison of AIMD results with IRMPD, it must be noted that the IRMPD mechanism involves the *noncoherent*, sequential absorption of multiple photons, with IVR mediated randomization of the internal vibrational energy between absorption events. Specifically for the IRMPD spectra obtained with a free-electron laser[47] as the light source in the study conducted in Ref. 10, the infrared light typically consists of a train of low-intensity (≈ 10 μJ) ≈ 1 ps micropulses with approximately 1 ns spacing. This spacing allows for deexcitation of the resonant mode by IVR in between micropulses, and the contribution of nonlinear, multiple-photon processes to the IRMPD spectrum is minimal. Thus, although the IRMPD process raises the internal vibrational energy of the ions to above the dissociation threshold, the critical step is the absorption of the first photon, which is why the resulting spectra represent the ions at their *initial* temperature.

A. Classical and quantum mechanical analysis of the shared proton distribution

To further probe the effect of temperature on the vibrational spectrum, we provide the distribution of oxygen-oxygen (OO) distances sampled during the finite temperature AIMD studies in Fig. 8. It is clear that the higher temperature simulations have a wider OO distribution. Furthermore, a one-dimensional slice of the potential surface encountered by the shared proton at various OO distances is also shown in red in Fig. 8. As can be seen the shared proton potential changes from a steep single well potential for smaller values of the OO distance (in the range of 2.3–2.4 Å) to a broad
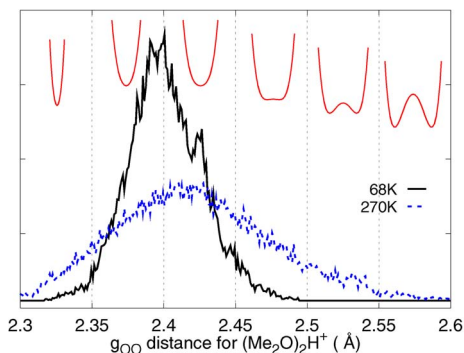
FIG. 8. (Color online) The oxygen-oxygen radial distribution function for $[Me_2O–H–OMe_2]^+$. A one-dimensional slice of the average potential encountered by the shared proton along the oxygen-oxygen axis is shown in red for each vertical slice. For example, the shared proton encounters an average double-well potential when the oxygen-oxygen distance is between 2.5 and 2.6 Å. On the contrary, the potential is a single well when the oxygen-oxygen distance is between 2.3 and 2.4 Å. This leads to the temperature dependence of the vibrational spectrum. The vertical spread of all the red curves is ≈3.8 kcal/mol.

calculations mainly sample the smaller values of OO distance, whereas the higher temperature calculations are influenced by the larger fluctuation in OO distance.

A qualitative understanding of the reordering of eigenstates is achieved upon inspection of the one-dimensional proton potentials parallel and perpendicular to the oxygen-oxygen axis. For smaller oxygen-oxygen distances, the one-dimensional proton potentials parallel to the oxygen-oxygen axis are more constraining and steeper as compared to the nature of the potential perpendicular to the oxygen-oxygen axis. This essentially raises the energy of states directed along the OO axis. For larger oxygen-oxygen distances, the situation is reversed and the proton potentials parallel to the oxygen-oxygen axis are less constraining as flatter single well and double well potentials are explored (see Fig. 8). As a result, as larger oxygen-oxygen distances are sampled, the transition frequency along the oxygen-oxygen axis gets lowered with respect to the transition perpendicular to the axis. Hence, the overall symmetry of the sampled potential surface changes at high temperatures which has an important impact on the observed and calculated vibrational spectra.

The findings in this section indicate that there is a strong correlation between the oxygen-oxygen distances sampled during finite temperature dynamics and the ordering of the shared proton eigenstates. These findings provide a qualitative measure of the difference in shared proton behavior at various temperatures. These results are, however, not to be confused with those obtained in the previous section, where the motions depicted involve *all* atoms in the system, while the conclusions presented here are germane to nuclear quantization involving only the shared proton.

and flat single well (through the range of 2.4–2.5 Å) and finally a double well potential for the large OO distances (in the range greater than 2.5 Å).

The effect of this fluctuation in OO distances on the trapped proton can be understood by analyzing the eigenstates of the quantized proton on each of the potentials depicted in Fig. 8. These computations are carried out through Arnoldi diagonalization of the three-dimensional proton Hamiltonian given in Eq. (7). The discretization is performed inside a box that is 1.0 Å wide along the OO direction as well as along the orthogonal directions. The potential energy surface is computed inside this box (on a regular grid) using the B3LYP/6-31+G** level of theory.

In Fig. 9, the evolution of the symmetric zero-point state (black), an excited "p-type" protonic vibrational state spread along the oxygen-oxygen axis (red), and an excited "p-type" state spread perpendicular to the oxygen-oxygen axis (blue) are shown with respect to OO distances encountered during AIMD. For small distances the state oriented along the oxygen-oxygen axis is actually higher in energy as compared to the state perpendicular to the axis, while the situation is reversed for larger distances. Clearly, this has an important influence in the spectral results since the lower temperature

IV. CONCLUSION

In order to understand the differences between single-photon argon-tagged action spectroscopy and IRMPD experiments, we consider a prototypical hydrogen bonded organic system, the proton bound dimethyl ether dimer, $(Me_2O)_2H^+$, which has been studied by several experiments[10,11,50] recently. It is noted that the spectral features differ in vibrational broadening depending on the experimental method used. In our study, we have utilized AIMD techniques, BOMD, and the ADMP, along with geometry optimization and harmonic frequency analysis at the DFT and post-Hartree Fock (MP2) levels of theory. In addition, we have also computed nuclear quantum effects arising from the shared proton as a function of different oxygen-oxygen, effective donor-acceptor "gating mode" distances. We have also assigned the finite temperature AIMD results at different temperatures to understand the differences between the spectra obtained at various AIMD temperatures.

To probe the spectroscopic signatures, we obtained the dynamically averaged spectra by computing the Fourier transform of both nuclear velocity (FT-VAC) and molecular dipole (FT-DAC) autocorrelation functions. We find that the low temperature AIMD results provide a qualitative explanation for the argon tagged action spectral results, whereas the higher temperature simulations present a good description of

FIG. 9. (Color online) Evolution of the shared proton zero point energy and excited states de-localized parallel (∥ in figure) and perpendicular (⊥ in figure) to the oxygen-oxygen axis are shown with increasing interoxygen distance for $(Me_2O)_2H^+$.

the IRMPD results. In order to spectroscopically assign the dynamically averaged, finite temperature AIMD spectral results, we project the FT-VAC onto a complete set of harmonic normal mode vectors. By doing so, we have resolved the doublet around 1000 cm^{-1} present in the argon-tagged single-photon spectrum (but not present in the normal mode harmonic spectral result) as occurring due to coupling between the backbone ether triatomic (COC) symmetric stretch, the oxygen-oxygen stretch, and the methyl wag modes with the shared proton stretch. These results are very much reminiscent of the recently resolved Zundel cation system where the coupling between the shared proton stretch and the motion of peripheral atoms[27] are responsible for splitting the 900 cm^{-1} singlet peak noted in earlier harmonic calculations.[5] Here, a similar contribution from the COC symmetric stretch and the methyl wag, in the proton-bound dimethyl ether dimer, the most fundamental organic Zundel-like system, results in splitting the sharp singlet at 940 cm^{-1} reported in the harmonic spectrum.

Our AIMD studies also indicate that the IRMPD results are broad in distribution due to the intrinsic higher ionic temperature. This allows the system to sample a broader range of the (anharmonic) potential energy surface which, in general, couples many more harmonic modes as compared to argon-tagged result. This aspect is clearly noted in our harmonic decomposition analysis of the temperature dependent vibrational density of states, where we find that both high and low temperature spectral features display a similar pattern of contributions from the underlying harmonic normal modes, i.e., both the low and high temperature results show a similar light mode distribution. However, the higher temperature results demonstrate a larger set of dark modes as compared to the lower temperature results. The intrinsic higher ionic temperature in IRMPD is further confirmed by computing nuclear quantum effects due to the shared proton, which suggests that at higher temperatures, a wider range of oxygen-oxygen distances are sampled. This changes the intrinsic form of the shared proton potential surface from a narrow, confining single well to a broader double-well-type potential. This kind of temperature assisted potential energy transformation has an important role on the IRMPD spectral result.

ACKNOWLEDGMENTS

APPENDIX: HARMONIC SPECTRAL ASSIGNMENTS

The harmonic spectral assignments and the glossary for the symbols utilized to depict these modes in the main manuscript can be found in Tables VI–IX. The arrows represent harmonic mode components. The mode symbols are arranged as $H_{\text{subscript}}^{\text{superscript}}$ where the subscript indicates the actual normal mode frequency and the superscript is a notation utilized to describe the mode. The mode is described in the tables both in text as well as pictorially.

TABLE VI. Notation used in the main text to describe the harmonic normal modes.

Symbol	Description	Mode
$H_{32}^{ether_{A-twist}}$	asymetric twist of the two methyl ether groups	
$H_{536}^{OO_S-COC_{S-S}}$	Oxygen-Oxygen stretch coupled to C-O-C backbone symmetric stretch	
$H_{788}^{OPO_{A-S}-COC_{S-S}}$	Oxygen-Proton-Oxygen three atom asymmetric stretch coupled to C-O-C backbone symmetric stretch	
$H_{932}^{OO_S-COC_{S-S}}$	oxygen-oxygen stretch coupled to C-O-C backbone symmetric stretch	
$H_{940}^{P_\parallel-COC_{S-S}}$	Shared proton stretch coupled to symmetric C-O-C stretch	
$H_{1041}^{COC_{A-S}-P_\perp}$	C-O-C asymmetric stretch coupled to proton motion perpendicular to oxygen-oxygen axis	
$H_{1041}^{COC_{A-S}-P_\perp}$	C-O-C asymmetric stretch coupled to proton motion perpendicular to oxygen-oxygen axis (orthogonal and degenerate to the previous mode)	
$H_{1147}^{CH3_{wag}-P_\perp}$	methyl group wag coupled to proton motion perpendicular to oxygen-oxygen axis	
$H_{1147}^{CH3_{wag}-P_\perp}$	methyl group wag coupled to proton motion perpendicular to oxygen-oxygen axis (orthogonal to the previous one)	

TABLE VII. Notation of harmonic modes used in the decomposition of dynamically averaged spectra.
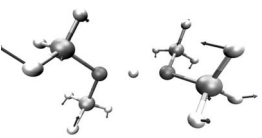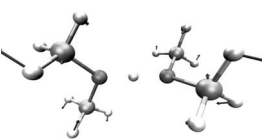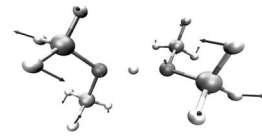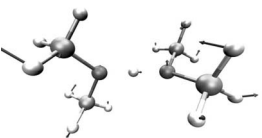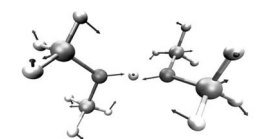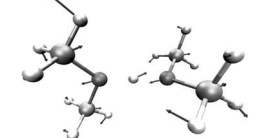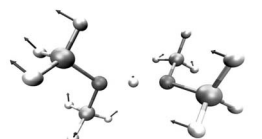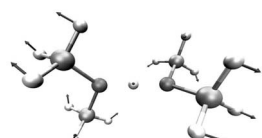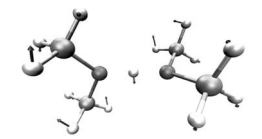
	Mode	Demonstration
$H_{1157}^{CH3_{S-wag}}$	symmetric wag in the two C-O-C backbone methyl groups	
$H_{1157}^{CH3_{S-wag}}$	symmetric wag in the two C-O-C backbone methyl groups(orthogonal to the previous one)	
$H_{1194}^{Ether_{wag}}$	Dimethyl ether wag	
$H_{1201}^{Ether_{wag}-P_{\parallel}}$	Dimethyl ether wag coupled to shared proton stretch	
$H_{1294}^{OO_{S}-CH3_{wag}}$	O-O stretch coupled to C-O-C backbone scissor, methyl wag and proton perpendicular motion	
$H_{1297}^{OPO_{A-S}-CH3_{rock}-COC_{scissor}}$	oxygen-proton-oxygen asymmetric stretch coupled to methyl rock and C-O-C backbone scissor	
$H_{1464}^{CH3_{A-umbrella}-P_{\perp}}$	asymmetric umbrella motion in the two C-O-C backbone methyl groups coupled to proton perpendicular	
$H_{1464}^{CH3_{A-umbrella}-P_{\perp}}$	asymmetric umbrella motion in the two C-O-C backbone methyl groups coupled to proton perpendicular(orthogonal to the previous one)	
$H_{1479}^{CH3_{A-scissor}-P_{\perp}}$	asymmetric scissor in two C-O-C backbone methyl groups coupled to proton perpendicular	

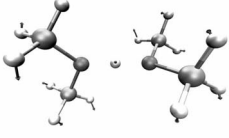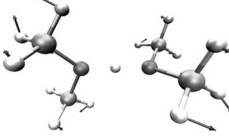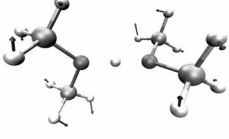TABLE VIII. Notation of harmonic modes used in the decomposition of dynamically averaged spectra.
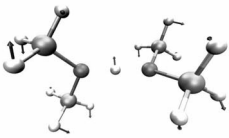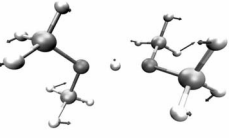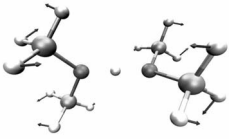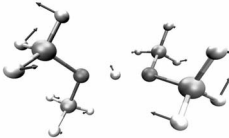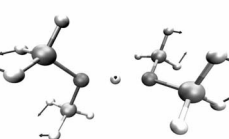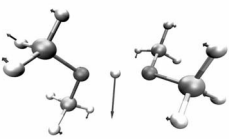
Symbol	Mode	Demonstration
$H^{CH3_{scissor-rock}}_{1493}$	scissor and rock in two C-O-C backbone methyl groups	
$H^{CH3_{scissor-rock}-P_\perp}_{1483}$	scissor and rock in the two C-O-C backbone methyl groups coupled to proton perpendicular	
$H^{CH3_{S-umbrella}}_{1492}$	symmetric umbrella motion of methyl groups	
$H^{CH3_{S-scissor}-P_\perp}_{1494}$	symmetric scissor in the two C-O-C backbone methyl groups coupled to proton perpendicular	
$H^{CH3_{A-scissor}-P_\perp}_{1497}$	assymetric scissor in the two C-O-C backbone methyl groups coupled to proton perpendicular	
$H^{CH3_{A-scissor}-P_\perp}_{1498}$	assymetric scissor in the two C-O-C backbone methyl groups coupled to proton perpendicular	
$H^{CH3_{scissor-rock}-P_\perp}_{1506}$	scissor and rock in the two C-O-C backbone methyl groups coupled to proton perpendicular	
$H^{CH3_{S-scissor}-P_\perp}_{1515}$	symmetric scissor in the two C-O-C backbone methyl groups coupled to proton perpendicular	
$H^{P_\perp}_{1521}$	proton perpendicular	

TABLE IX. Notation of harmonic modes used in the decomposition of dynamically averaged spectra.

	Mode	Demonstration
$H_{1547}^{P_\perp}$	proton perpendicular	
$H_{1555}^{P_\searrow + CH3_{S-scissor}}$	Proton diagonal motion and symmetric scissor in the two C-O-C backbone methyl groups	
$H_{3163}^{S-CH_{stretch}}$	in-phase C-H stretch in the two methyl groups on the C-O-C backbone	
$H_{3166}^{A-CH_{stretch}}$	out-of-phase C-H stretch in the two methyl groups on the C-O-C backbone	
$H_{3192}^{CH_{stretch}}$	C-H stretch	
$H_{3192}^{CH_{stretch}}$	C-H stretch	

[1] J.-W. Shin, N. I. Hammer, E. G. Diken, M. A. Johnson, R. S. Walters, T. D. Jaeger, M. A. Duncan, R. A. Christie, and K. D. Jordan, Science **304**, 1137 (2004).

[2] M. Miyazaki, A. Fujii, T. Ebata, and N. Mikami, Science **304**, 1134 (2004).

[3] T. S. Zwier, Science **304**, 1119 (2004).

[4] M. Okumura, L. I. Yeh, J. D. Myers, and Y. T. Lee, J. Phys. Chem. **94**, 3416 (1990).

[5] X. Yang, X. Zhang, and A. W. Castleman, Jr., Int. J. Mass Spectrom. Ion Process. **109**, 339 (1991).

[6] E. G. Diken, J. M. Headrick, J. R. Roscioli, J. C. Bopp, M. A. Johnson, and A. B. McCoy, J. Phys. Chem. A **109**, 1487 (2005).

[7] K. R. Asmis, N. L. Pivonka, G. Santambrogio, M. Brümmer, C. Kaposta, D. M. Neumark, and L. Wöste, Science **299**, 1375 (2003).

[8] N. I. Hammer, E. G. Diken, J. R. Roscioli, M. A. Johnson, E. M. Myshakin, K. D. Jordan, A. B. McCoy, X. Huang, J. M. Bowman, and S. Carter, J. Chem. Phys. **122**, 244301 (2005).

[9] A. W. Castleman and R. G. Keesee, Chem. Rev. (Washington, D.C.) **86**, 589 (1986).

[10] D. T. Moore, J. Oomens, L. van der Meer, G. von Helden, G. Meijer, J. Valle, A. G. Marshall, and J. R. Eyler, ChemPhysChem **5**, 740 (2004).

[11] J. R. Roscioli, L. R. McCunn, and M. A. Johnson, Science **316**, 249 (2007).

[12] N. Agmon, Chem. Phys. Lett. **244**, 456 (1995).

[13] H.-P. Cheng, J. Phys. Chem. A **102**, 6201 (1998).

[14] D. Wei and D. R. Salahub, J. Chem. Phys. **106**, 6086 (1997).

[15] C. J. Tsai and K. D. Jordan, Chem. Phys. Lett. **213**, 181 (1993).

[16] S. S. Xantheas, J. Chem. Phys. **100**, 7523 (1994).

[17] E. S. Kryachko, Chem. Phys. Lett. **314**, 353 (1999).

[18] R. Pomes and B. Roux, J. Phys. Chem. **100**, 2519 (1996).

[19] H. Decornez, K. Drukker, and S. Hammes-Schiffer, J. Phys. Chem. A **103**, 2891 (1999).

[20] M. L. Brewer, U. W. Schmitt, and G. A. Voth, Biophys. J. **80**, 1691 (2001).

[21] S. S. Iyengar, J. Chem. Phys. **126**, 216101 (2007).

[22] S. S. Iyengar, M. K. Petersen, T. J. F. Day, C. J. Burnham, V. E. Teige, and G. A. Voth, J. Chem. Phys. **123**, 084309 (2005).

[23] C.-C. Wu, C.-K. Lin, H.-C. Chang, J.-C. Jiang, J.-L. Kuo, and M. L. Klein, J. Chem. Phys. **122**, 074315 (2005).

[24] S. S. Iyengar, T. J. F. Day, and G. A. Voth, Int. J. Mass. Spectrom. **241**, 197 (2005).

[25] X. Li, V. E. Teige, and S. S. Iyengar, J. Phys. Chem. A **111**, 4815 (2007).

[26] S. S. Iyengar, J. Chem. Phys. **123**, 084310 (2005).

[27] O. Vendrell, F. Gatti, and H.-D. Meyer, Angew. Chem., Int. Ed. **46**, 6918 (2007).

[28] M. Kaledin, A. L. Kaledin, and J. M. Bowman, J. Phys. Chem. A **110**, 2922 (2006).

[29] A. B. McCoy, X. Huang, S. Carter, and J. M. Bowman, J. Chem. Phys. **123**, 064317 2005).

[30] J. M. Headrick, E. G. Diken, R. S. Walters, N. I. Hammer, R. A. Christie,

J. Cui, E. M. Myshakin, M. A. Duncan, M. A. Johnson, and K. Jordan, Science **308**, 1765 (2005).

[31] M. M. Teeter, Proc. Natl. Acad. Sci. U.S.A. **81**, 6014 (1984).

[32] S. Neidle, H. M. Berman, and H. S. Shieh, Nature (London) **288**, 129 (1980).

[33] L. A. Lipscomb, M. E. Peek, F. X. Zhou, J. A. Bertrand, D. Van Derveer, and L. D. Williams, Biochemistry **33**, 3649 (1994).

[34] W. W. Cleland and M. M. Kreevoy, Science **264**, 1887 (1994).

[35] A. Warshel, A. Papazyan, and P. A. Kollman, Science **269**, 102 (1995).

[36] V. E. Bondybey and M. K. Beyer, Int. Rev. Phys. Chem. **21**, 277 (2002).

[37] S. M. Haile, D. A. Boysen, C. R. I. Chisholm, and R. B. Merle, Nature (London) **410**, 910 (2001).

[38] M. Iannuzzi and M. Parrinello, Phys. Rev. Lett. **93**, 025901 (2004).

[39] M. J. McEwan and L. F. Phillips, *Chemistry of the Atmosphere* (Eward Arnold, London, 1975).

[40] B. J. Gertner and J. T. Hynes, Science **271**, 1563 (1996).

[41] J. P. Devlin, N. Uras, J. Sadlej, and V. Buch, Nature (London) **417**, 269 (2002).

[42] J. S. Aloisio and S. Francisco, Acc. Chem. Res. **33**, 825 (2000).

[43] M. K. Petersen, S. S. Iyengar, T. J. F. Day, and G. A. Voth, J. Phys. Chem. B **108**, 14804 (2004).

[44] D. Marx, M. E. Tuckerman, J. Hutter, and M. Parrinello, Nature (London) **397**, 601 (1999).

[45] M. E. Tuckerman, D. Marx, and M. Parrinello, Nature (London) **417**, 925 (2002).

[46] D. Asthagiri, L. R. Pratt, J. D. Kress, and M. A. Gomez, Proc. Natl. Acad. Sci. U.S.A. **101**, 7229 (2004).

[47] J. J. Valle, J. R. Eyler, J. Oomens, D. T. Moore, A. F. G. van der Meer, G. von Helden, G. Meijer, C. L. Hendrickson, A. G. Marshall, and G. T. Blakney, Rev. Sci. Instrum. **76**, 023103 (2005).

[48] M. F. Bush, M. W. Forbes, R. A. Jockusch, J. Oomens, N. C. Polfer, R. Saykally, and E. Williams, J. Phys. Chem. A **111**, 7753 (2007).

[49] N. L. Pivonka, C. Kaposta, M. Brummer, G. von Helden, G. Meijer, L. Woste, D. M. Neumark, and K. R. Asmis, J. Chem. Phys. **118**, 5275 (2003).

[50] T. D. Fridgen, P. MacAleese, L. Maitre, T. B. McMahon, P. Boissel, and J. Lemaire, Phys. Chem. Chem. Phys. **7**, 2747 (2005).

[51] M. E. Tuckerman, K. Laasonen, M. Sprik, and M. Parrinello, J. Phys. Chem. **99**, 5749 (1995).

[52] W. H. Robertson, E. G. Diken, E. A. Price, J.-W. Shin, and M. A. Johnson, Science **299**, 1367 (2003).

[53] E. G. Diken, J. M. Headrick, J. R. Roscioli, J. C. Bopp, M. A. Johnson, A. B. McCoy, X. Huang, S. Carter, and J. M. Bowman, J. Phys. Chem. A **109**, 571 (2005).

[54] J. Roscioli, E. Diken, M. Johnson, S. Horvath, and A. McCoy, J. Phys. Chem. A **110**, 4943 (2006).

[55] C. Swalina and S. Hammes-Schiffer, J. Phys. Chem. A **109**, 10410 (2005).

[56] I. Sumner and S. S. Iyengar, J. Phys. Chem. A **111**, 10313 (2007).

[57] J. M. Bowman, Acc. Chem. Res. **19**, 202 (1986).

[58] R. B. Gerber and M. A. Ratner, J. Chem. Phys. **70**, 97 (1988).

[59] J. O. Jung and R. B. Gerber, J. Chem. Phys. **105**, 10332 (1996).

[60] N. Matsunaga, G. M. Chaban, and R. B. Gerber, J. Chem. Phys. **117**, 3541 (2002).

[61] J. H. Skone, M. V. Pak, and S. Hammes-Schiffer, J. Chem. Phys. **123**, 134108 (2005).

[62] B. G. Levine and T. J. Martinez, Annu. Rev. Phys. Chem. **58**, 613 (2007).

[63] S. S. Iyengar, X. Li, and I. Sumner, Adv. Quantum Chem. **55** (2008).

[64] I. S. Y. Wang and M. Karplus, J. Am. Chem. Soc. **95**, 8160 (1973).

[65] C. Leforestier, J. Chem. Phys. **68**, 4406 (1978).

[66] K. Bolton, W. L. Hase, and G. H. Peslherbe, *Modern Methods for Multidimensional Dynamics Computation in Chemistry* (World Scientific, Singapore, 1998), p. 143.

[67] M. C. Payne, M. P. Teter, D. C. Allan, T. A. Arias, and J. D. Joannopoulos, Rev. Mod. Phys. **64**, 1045 (1992).

[68] H. B. Schlegel, J. M. Millam, S. S. Iyengar, G. A. Voth, A. D. Daniels, G. E. Scuseria, and M. J. Frisch, J. Chem. Phys. **114**, 9758 (2001).

[69] S. S. Iyengar, H. B. Schlegel, J. M. Millam, G. A. Voth, G. E. Scuseria, and M. J. Frisch, J. Chem. Phys. **115**, 10291 (2001).

[70] H. B. Schlegel, S. S. Iyengar, X. Li, J. M. Millam, G. A. Voth, G. E. Scuseria, and M. J. Frisch, J. Chem. Phys. **117**, 8694 (2002).

[71] S. S. Iyengar, H. B. Schlegel, G. A. Voth, J. M. Millam, G. E. Scuseria, and M. J. Frisch, Isr. J. Chem. **42**, 191 (2002).

[72] S. S. Iyengar and M. J. Frisch, J. Chem. Phys. **121**, 5061 (2004).

[73] M. J. Frisch, G. W. Trucks, H. B. Schlegel *et al.*, GAUSSIAN 03, Revision b.02, Gaussian, Inc., Pittsburgh, PA, 2003.

[74] D. Svozil and P. Jungwirth, J. Phys. Chem. A **110**, 9194 (2006).

[75] S. Sadhukhan, D. Munoz, C. Adamo, and G. E. Scuseria, Chem. Phys. Lett. **306**, 83 (1999).

[76] W. H. Press, S. A. Teukolsky, W. T. Vetterling, and B. P. Flannery, *Numerical Recipes in C* (Cambridge University Press, New York, 1992).

[77] S. S. Iyengar and J. Jakowski, J. Chem. Phys. **122**, 114105 (2005).

[78] S. S. Iyengar, Theor. Chem. Acc. **116**, 326 (2006).

[79] D. K. Hoffman, N. Nayar, O. A. Sharafeddin, and D. J. Kouri, J. Phys. Chem. **95**, 8299 (1991).

[80] D. J. Kouri, Y. Huang, and D. K. Hoffman, Phys. Rev. Lett. **75**, 49 (1995).

[81] J. Jakowski, I. Sumner, and S. S. Iyengar, J. Chem. Theory Comput. **2**, 1203 (2006).

[82] D. C. Sorensen, SIAM J. Matrix Anal. Appl. **13**, 357 (1992).

[83] G. H. Golub and C. F. van Loan, *Matrix Computations* (The Johns Hopkins University Press, Baltimore, 1996).

[84] B. N. Parlett and Y. Saad, Linear Algebr. Appl. **88/89**, 575 (1987).

[85] In Ref. 10, the following steps were involved in formation of the proton bound diether. First, methyl ether was ionized through electron impact. The ion population is rapidly (within a milliseconds) transferred to protonated methyl ether monomer by ion-molecule reactions, which is then converted to the ether dimer through addition of a second pulse of methyl ether vapor to the trap. Spontaneous, dark dissociation of the dimers is then utilized to monitor "temperature." The spontaneous dissociation (smoothly) decays below measurable values within a matter of seconds, which is an indication that the ions had reached (radiative) thermal equilibrium with the blackbody radiation from the (room temperature) vacuum chamber.

[86] A. Kohen, R. Cannio, S. Bartolucci, and J. P. Klinman, Nature (London) **399**, 496 (1999).